Orientation processing by synaptic integration across first-order tactile neurons

Etay Hay and J Andrew Pruszynski

[1]Department of Physiology and Pharmacology, [2]Brain and Mind Institute, [3]Robarts Research Institute, Western University, London, Canada

Abstract

Our ability to manipulate objects relies on tactile inputs signaled by first-order tactile neurons that innervate the glabrous skin of the hand. A fundamental feature of these first-order tactile neurons is that their distal axon branches in the skin and innervates many mechanoreceptive end organs, yielding spatially-complex receptive fields with several highly sensitive zones. Recent work indicates that this peripheral arrangement constitutes a neural mechanism enabling first-order tactile neurons to signal high-level geometric features of touched objects, such as the orientation of an edge moving across the skin. Here we show how second-order tactile neurons could integrate these complex peripheral signals to compute edge-orientation. We first derive spiking models of human first-order tactile neurons that fit and predict responses to moving edges with high accuracy. Importantly, our models suggest that first-order tactile neurons innervate mechanoreceptors in the fingertips following a random sampling scheme. We then use the model neurons as the basis for a simulation of the peripheral neuronal population and its synaptic integration by second-order tactile neurons (i.e. in the spinal cord and brainstem). Our model networks indicate that computations done by second-order neurons could underlie the human ability to process edge orientations with high acuity and speed. In particular, our models suggest that synaptic integration of AMPA inputs within short timescales is critical for discriminating fine orientations, whereas NMDA-like synapses refine discrimination and maintain robustness over longer timescales. Taken together, our results provide new insight into the computations occurring in the earliest stages of the human tactile processing pathway and how they may be critical for supporting hand function.

Correspondence:
Dr. Etay Hay
The Brain and Mind Institute
Western University
1151 Richmond St
London, Ontario, Canada
N6A 3K7
Email: etay.hay@uwo.ca

Introduction

Tactile input from the hands is important for many behaviors, ranging from daily motor tasks like buttoning a shirt to complex skills like knitting a sock [1]. This tactile information is conveyed by four types of first-order tactile neurons that innervate distinct mechanoreceptive end organs in the glabrous skin of the hand [2]. Of particular note are fast-adapting type 1 neurons (FA-1) innervating Meissner corpuscles and slow-adapting type 1 neurons (SA-1) innervating Merkel discs, which are particularly important for extracting fine spatial details of touched objects [3]. A fundamental feature of FA-1 and SA-1 neurons is that their axon branches in the skin and innervates many mechanoreceptors, ~30 on average [4], and thus these neurons have spatially-complex receptive fields with many highly-sensitive zones [3,5–7]. We have recently proposed that this innervation pattern may constitute a peripheral neural mechanism for extracting geometric features of touched objects [6].

Here we examine how the geometric features of touched objects are encoded by the population of first-order tactile neurons and the synaptic integration occurring at the level of second-order tactile neurons (in the spinal cord and cuneate nucleus [8]). Our approach differs from previous studies [9–13] in several ways. First, our models are based on first-order tactile neurons that have spatially complex receptive fields. Second, our models are constrained by neural recordings in humans, whereas previous models used data from monkeys [10,11]. Third, previous models of the peripheral neuronal population innervating the fingertips [9,12,14] examined encoding of stimuli using abstract features of its response, such as mean firing rate, spike count or first-spike latency. Other models examined the evolution of synaptic weights between first- and second-order neurons over stimulus presentations but did not address the encoding of the stimuli [13]. In contrast, our models examine the encoding of tactile stimuli using synaptic integration at the level of second-order neurons, and thus provide mechanistic insight into how upstream neurons extract meaningful tactile information from the complex responses of the peripheral neuronal population.

We provide new insights both at the level of single neurons and the neuronal population. At the level of single neurons, we derive spiking models of first-order tactile neurons that fit and predict empirical data with good accuracy. We then use these model neurons to delineate the number of mechanoreceptors innervated by first-order tactile neurons, and suggest that mechanoreceptor innervation follows a random-sampling scheme. At the level of the neuronal

population, we investigate the computational capabilities afforded second-order tactile neurons by integrating synaptic inputs from the periphery. We show that computations performed by second-order neurons can account for the human ability to discriminate tactile edge orientations with high acuity (< 3˚) and speed [15]. Our results suggest that discriminating edge orientation in this manner relies on a small number of key connections from first-order neurons. Our results also suggest that integrating AMPA-like synaptic input over a short time scale (i.e. coincidence detection) is critical for robustly discriminating with high acuity whereas integrating NMDA-like synaptic input serves to refine discrimination and maintain robustness over longer time scales (i.e. temporal summation).

Results

Data-driven models of first-order tactile neurons

We generated spiking models of human FA-1 neurons (n = 17 neurons) constrained by their response to oriented edges moving across the fingertip. Each model neuron innervated a set of model mechanoreceptors which were constrained to lie within the boundary of the recorded neuron's receptive field (Figure 1A). Model mechanoreceptors could differ in weight, causing model neurons to have spatially-complex receptive fields (Figure 1B). The output of each model mechanoreceptor depended on its distance from the stimulus (Figure 1C). Spikes were generated at each model mechanoreceptor and followed a linear relationship between model mechanoreceptor output and spike rate, along with spike rate saturation (Figure 1D). Spiking outputs also exhibited adaptation (Figure 1E) and resetting (Figure 1F) as described in the Methods. The free parameters were the location of the model mechanoreceptors innervated by the model neuron, the output weight of each model mechanoreceptor, and the maximal spike rate of the model neuron. We used a genetic algorithm to search for the parameter values that best fitted the spike data (see Methods).

We constrained the models with empirical spike responses to edges at five different orientations relative to their movement direction (0, ±22.5, ±45˚). Optimization with our genetic algorithm yielded models that fit the data with high accuracy (R^2 = 88 ± 5%, mean ± SD, n = 17 neurons, Figure 2A,D). When tested with data from a different edge orientation not used to fit the model (30˚), the models predicted the spike response well (R^2 = 69 ± 11%, Figure 2C,D), and significantly better than null models in which the mechanoreceptor locations were shuffled across

the recorded neuron's receptive field boundary (R^2 = 38 ± 15%, n = 17, $p < 10^{-6}$, paired-sample t-test, Figure 2D).

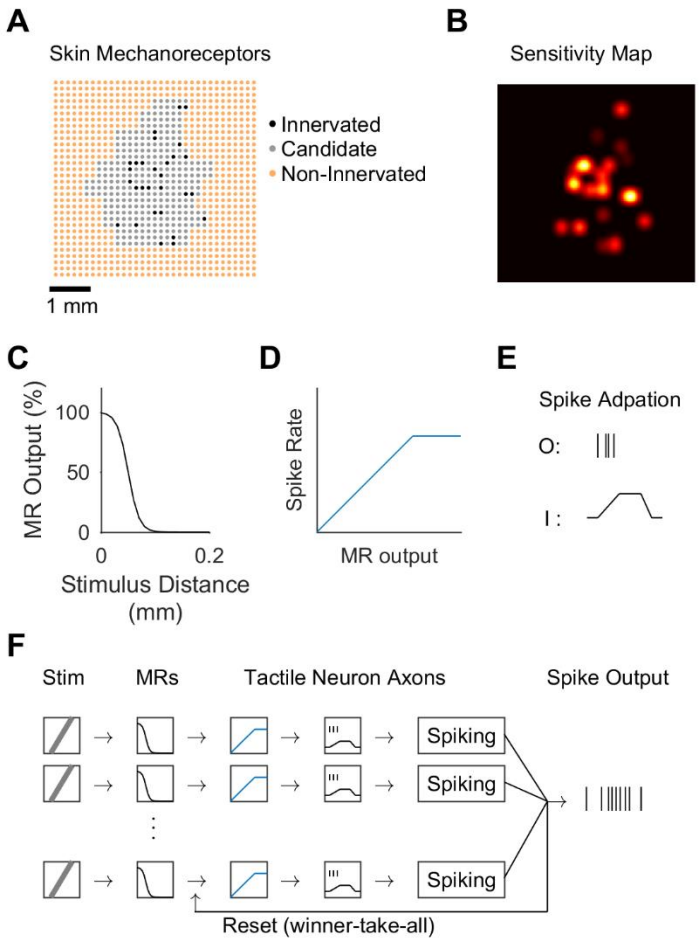

Figure 1. Modeling framework for first-order tactile neurons. A. Receptive field was modeled as a grid of mechanoreceptors. The area enclosing candidate mechanoreceptors (gray) was derived from the recorded neuron's response to a moving dot stimulus (see Methods). The model neuron innervated a subset of model mechanoreceptors (black). **B.** Receptive field sensitivity map, showing the different output weights of the model mechanoreceptors. **C.** The output of each model mechanoreceptor (MR) as a function of its distance from the stimulus. **D.** The rate of spikes generated at each model mechanoreceptor as a function of the model mechanoreceptor output. **E.** Spike train adaptation yielded spiking only when the input was increasing. **F.** Complete schematic of a model neuron. Note that spikes generated at one model mechanoreceptor initiation zone reset spike generation at the other spike initiation zones, resulting in a winner-take-all (max) spike rate.

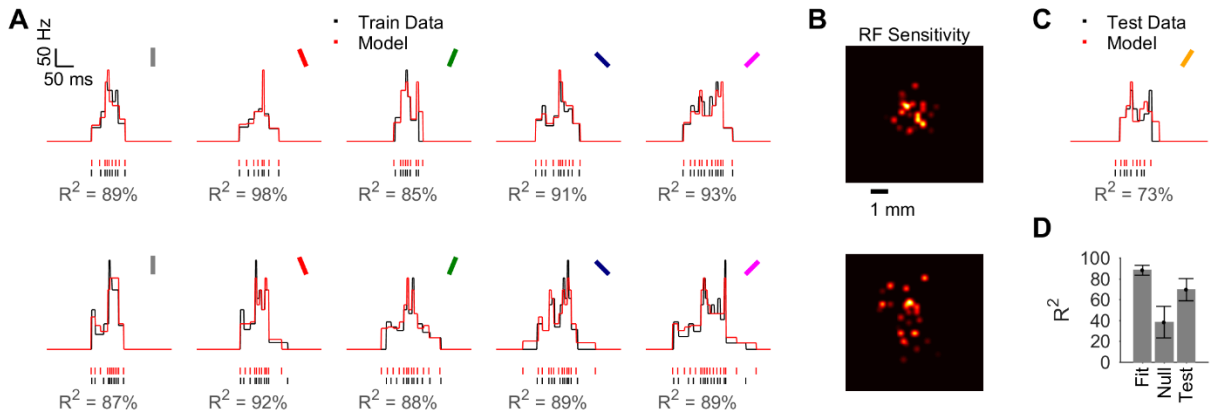

Figure 2. Data-driven model fitness and prediction accuracy. A. Fitness (R^2) of models for two example FA-1 neurons (top and bottom rows). Observed (black) and model (red) spike trains and rate curves in response to edges oriented 0, -22.5, 22.5, -45, and 45˚. **B.** The derived receptive field sensitivity (normalized) for the two model neurons. **C.** Observed and model response to edge oriented 30˚, which served to test the models. **D.** Model fitness, prediction accuracy, and the prediction accuracy of null models (shuffled, see Methods) across all neurons (n = 17). Prediction accuracy of models was significantly higher than that of null models ($p < 10^{-6}$, paired-sample t-test). Error bars depict standard deviation.

We next investigated how many mechanoreceptors were necessary for high model fitness, by optimizing the models using sets of mechanoreceptors ranging in number from 5 to 50 (Figure 3A). We defined fitness saturation as the point beyond which the difference in average model fitness across the five edge orientations was less than 1%. Model fitness increased with the number of available mechanoreceptors, but saturated on average at 28 ± 11 mechanoreceptors. We found no significant correlation between the size of the model receptive field area and the required number of mechanoreceptors ($r = 0.42$, $p = 0.09$, Figure 3B).

The distribution of model mechanoreceptor weights tended to be linearly decreasing (Figure 3C). We defined mechanoreceptor hotspots as model mechanoreceptors that provided particularly large input (top 25%), and we inspected whether these hotspots tended to cluster spatially, by comparing the nearest-neighbor distance between hotspots to the distance between random subsets of all mechanoreceptors within the receptive field boundary (see Methods). The nearest-neighbor distance between hotspots was 0.63 ± 0.3 mm, and the chance distance was 0.69 ± 0.22 (Figure 3D). The difference between the two was not statistically significant (mean difference was 0.06 mm, 95% confidence interval -0.01 – 0.21 mm), indicating that hotspots did not tend to cluster. Similarly, model mechanoreceptors in general did not tend to cluster (mean

difference between nearest-neighbor distance of model mechanoreceptors and chance was 0.01 mm, 95% confidence interval 0 – 0.03 mm).

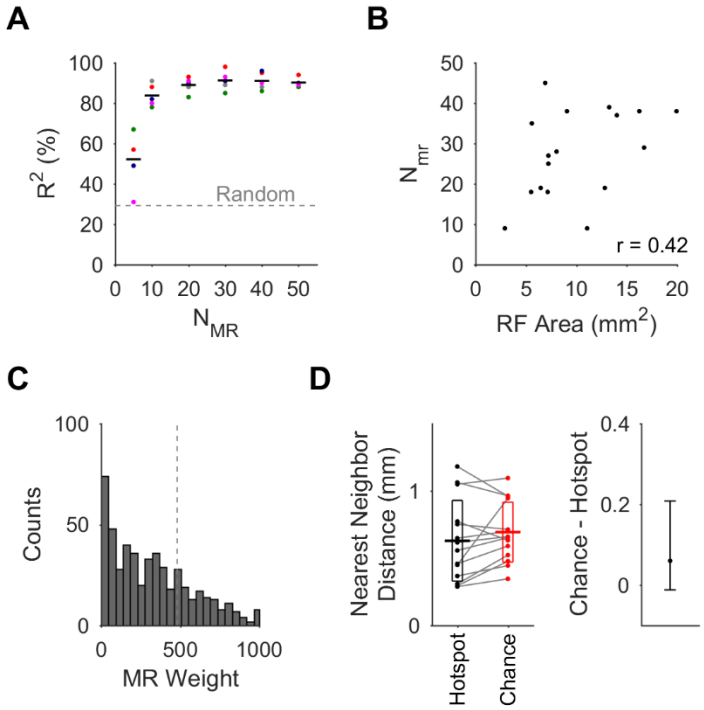

Figure 3. Mechanoreceptors innervation in the data-driven models. A. Model fitness for an example neuron, as a function of the maximal number of mechanoreceptors available during the optimization. Each dot corresponds to the model fitness for a different edge orientation, color-coded as in Figure 2, and the black bar denotes the average fitness. Dashed gray line denotes the fitness of null models. **B.** The number of mechanoreceptors where model fitness saturated as a function of the receptive field area. **C.** Distribution of model mechanoreceptor weights over all model neurons. Mechanoreceptors that provided large input (top 25%, dashed line) were termed hotspots. **D.** Left - nearest neighbor distance between hotspots (black) or between random subsets of mechanoreceptors within the boundaries of the receptive field (red) for each model neuron. Boxes show 95% confidence intervals. Right – 95% confidence intervals of the difference between chance and hotspot distance, indicating that the two were not significantly different. (n = 17 neurons for B-D).

Encoding edge orientation via synaptic integration of first-order neuronal population activity

We next determined whether the activity of FA-1 neuronal population can be used by second-order neurons to discriminate edge orientations accurately. We simulated a model population of 292 FA-1 neurons innervating a 10x10 mm patch of skin. We generated the model

neuron population as randomized variations of the 17 model neurons (see Methods). Randomization was motivated by our finding that innervation hotspots seemed to be randomly distributed within the area of responsivity (Figure 3D).

We simulated the population response to oriented edges passing over the skin patch (Figure 4A). The response of the first-order population was then convolved with a postsynaptic potential (PSP) waveform and fed into a layer of second-order neurons (in spinal cord or cuneate), performing synaptic integration. The task was to discriminate between two edges oriented at $\pm\theta$ (where θ = 1, 3, 5, 10, or 20˚), where classification was determined by a winner-take-all (max) across the second-order neurons.

We inspected the discrimination accuracy of the model second-order neurons using PSPs of different decay time constants – either a short time constant corresponding to AMPA synapses (τ_{decay} = 3 ms), a long time constant corresponding to NMDA synapses (τ_{decay} = 65 ms), or a combination of both (Figure 4B). We trained the second-order neuron classifiers using a genetic algorithm to find the weights between first-order and second-order neurons that best discriminated edge orientations. We then tested the discrimination accuracy of model second-order neurons under different levels of stimulus noise (0 – 10%, see Methods). In the noiseless case, we found that the activity in the first-order population could be used to discriminate different edge orientations perfectly with high acuity (to within ±1˚), for either of the PSP time constants (Figure 4C,D). When adding noise to the stimulus, the discrimination accuracy of model second-order neurons remained high (80-90% success), although discrimination became challenging for finer orientations. Discrimination accuracy using NMDA-like synapses was more robust to noise, compared to using AMPA-like synapses (improving test performance by 10 – 20%), except for the finest orientation of ±1˚, for which the two synaptic types fared similarly (Figure 4E). Using a combination of AMPA- and NMDA-like PSPs did not significantly improve the robustness to noise.

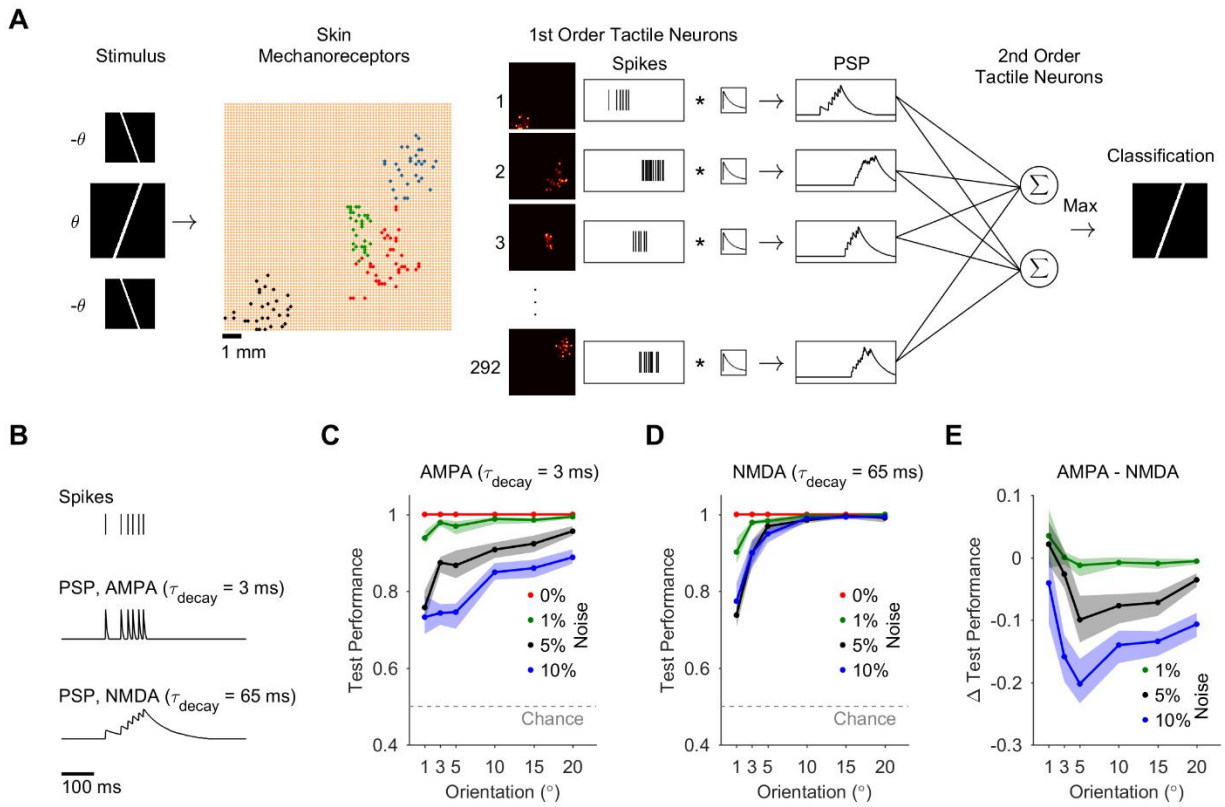

Figure 4. Discrimination of edge orientation using synaptic integration of first-order population activity. A. Simulated model neuronal network, where the first layer was the population of FA-1 neurons innervating mechanoreceptors in a 10x10 mm patch of skin. The next layer was second-order neurons, modeled as performing synaptic integration of inputs from first-order neurons with a winner-take-all (max) scheme. Four example model first-order neurons are shown as color-coded sets of model mechanoreceptors on the skin grid, with their corresponding spike trains to the right. **B.** PSPs were produced by convolving model first-order neuronal spike trains with a PSP waveform using either a short time constant (3 ms, corresponding to AMPA synapses) or a long time constant (65 ms, corresponding to NMDA synapses). **C, D.** Discrimination test performance of model second-order neurons using AMPA-like (C) or NMDA-like (D) synapses. Each curve corresponds to a different level of stimulus noise (between 0 and 10%), and shows mean and 95% confidence intervals. Dashed gray line shows chance level (0.5). **E.** The difference in test performance between model networks using AMPA-like and NMDA-like synapses, for noise level 1, 5, 10%.

We next varied the stimulation presentation time window (5, 10, 20, 50, 100 ms, and unlimited, see Methods) and examined its effect on discrimination accuracy. In the noiseless case, the discrimination accuracy of model second-order neurons remained perfect regardless of the synaptic receptor type or time window size. However, when noise was applied, discrimination was more robust over shorter time windows for both AMPA-like and NMDA-like synapses (Figure

5A). Moreover, integrating inputs using AMPA-like synapses over a short time window (5 ms) improved robustness to noise when discriminating fine orientations (±1˚) better than when using NMDA, increasing test performance by ~10% (Figure 5B, D). Overall, performance of model second-order neurons that used AMPA-like synapses increased significantly in the case of short time window compared to long time window (Figure 5C vs Figure 4C), approaching the robustness of NMDA-like synapses over all orientations and improving performance for fine orientations (Figure 5D).

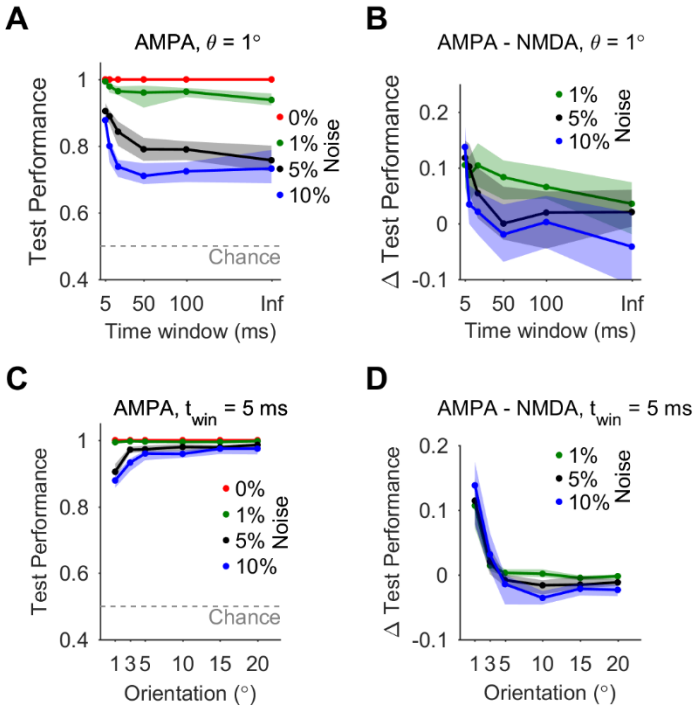

Figure 5. AMPA integration over short time window robustly discriminates fine orientations. A. Discrimination test performance of model second-order neurons as a function of stimulus presentation time window, for fine orientations (θ = ±1˚) and using AMPA-like synapses. **B.** The difference in test performance between model second-order neurons using AMPA-like and NMDA-like synapses for fine orientations (θ = ±1˚), as a function of presentation time window, for noise level 1, 5, 10%. **C.** Discrimination test performance for model second-order neurons over all orientations, using short integration time window (5 ms) and AMPA-like synapses. **D.** The difference in test performance between model second-order neurons using AMPA and NMDA, for integration time window of 5 ms and noise level 1, 5, 10%.

To inspect the connectivity in the model network between first- and second-order neurons underlying discrimination of different edges, we examined the connection weights and their spatial layout. Connection weights from most first-order neurons were close to 0 on average, and only a

small subset of model first-order neurons consistently provided a large input (Figure 6A, based on 95% confidence intervals estimated by bootstrapping weights from 20 randomized trained networks, corrected for multiple comparisons). The number of key connections was 10 ± 5 (across different stimulus angles). We found no significant correlation between the stimulus angle and the number of key connections (r = -0.03, p = 0.96). The weights of the key excitatory connections were anticorrelated between model second-order neurons tuned to opposite orientations (Figure 6B, r = -0.87, p < 0.001). This was seen also in the receptive field map of the model second-order neurons, which exhibited areas of positive and null sensitivity that alternated between oppositely-tuned neurons (Figure 6C). In addition, the receptive field map showed that the model neurons relied on coincidence of activation from distal parts of the edge stimulus, where the difference between opposite edges is largest.

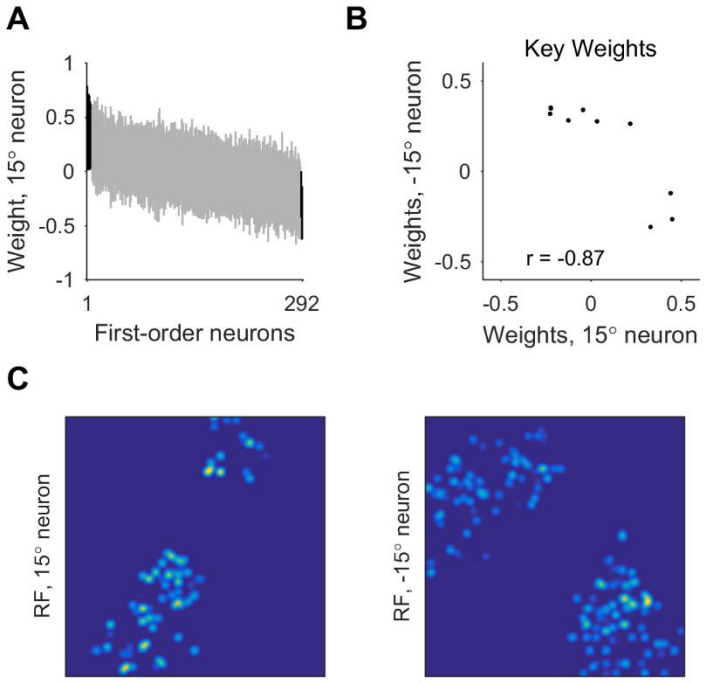

Figure 6. Connection weights and receptive field of model second-order neurons. A. Model weights from first-order tactile neurons onto second-order neurons tuned to 15˚, with presentation time window of 50 ms and noise level 10%. Shown are 95% confidence intervals of weights over 20 model networks. Weights are shown in decreasing order of average weight over the 20 model networks. Black – key weights, which were significantly different than 0. **B.** Key excitatory weights in model second-order neurons tuned to 15 vs -15˚. **C.** Spatial layout of the key excitatory weights in the receptive field of model second-order neurons tuned to -15 or 15˚, with presentation time window of 50 ms and noise level 10%. Receptive fields represent averages over 20 model networks.

Discussion

Our study provides new insight into tactile processing both at the level of single first-order tactile neurons and at the level of the neuronal population. We derived spiking models of human FA-1 neurons innervating mechanoreceptors in the fingertips that were able to fit and predict responses to oriented edge stimuli with high accuracy. Importantly, these models predict that first-order tactile neurons innervate mechanoreceptors following a random sampling scheme consistent with efficient strategies for extracting stimulus features. We then simulated first-order population activity from the fingertip and its synaptic integration by second-order neurons. Importantly, our model networks predict that computations at the level of second order neurons in the brainstem and/or spinal cord could underlie the ability of humans to use edge-orientation information with high acuity and speed, as in the context of hand control.

Our single-neuron models required ~30 mechanoreceptors on average to fit the spike response, which agrees with previous empirical estimates of the number of Meissner corpuscles converging onto a single FA-1 neuron [4]. Moreover, our models predict that mechanoreceptors (all of them as well as only particularly potent ones) are randomly scattered within the boundaries of the receptive field. Under the constraint of convergence (many receptors to each first-order neuron), random sampling by a relatively small number of neurons can take advantage of the sparseness of natural stimuli to efficiently extract stimulus features – a strategy termed compressed sensing [16–20]. Evidence for compressed sensing has been reported in olfaction [21,22] and our results support the idea that this is a general principle of peripheral sensory pathways.

Despite using a winner-take-all (max) spiking scheme [23–25], our models exhibit a variety of peak rates in response to different edge orientations, consistent with previous empirical results [6,7]. This richness arises because neuronal spike output is not only a function of the present input but also of the neuron's previous spikes – a demonstration of how spiking increases a neuron's computational power [26]. It remains to be seen if a winner-take-all scheme applies to other first-order tactile neurons, or in response to stimuli of lower intensity, which could instead involve a "mixing" of the spike trains [27]. Our models include skin mechanics only implicitly. Although this simplification was sufficient for fitting and predicting spike responses in our data, our data-driven model optimization framework can be extended to include explicit components of skin dynamics as used in other tactile neuron models [11,25]. We have implemented noise at the level of the stimulus. The response of FA-1 and second-order cuneate neurons shows little variability

[28–30], therefore there seems to be no significant noise at the level of mechanoreceptor to first-order neuron, or first- and second-order neuron connections. While stimulus noise in the experimental data was < 1%, the larger levels of noise that we have investigated could relate to other sources of noise such as variability in finger positioning during tasks. These in turn can account for the behavioral noise measured in tactile discrimination tasks [15].

The readout of first-order population activity by second-order neurons in our model networks involves synaptic integration, thus providing additional mechanistic insight unavailable to previous models that compute using abstract features of the population response such as mean firing rate, spike count, or spike latency [9–12]. That is, models based on abstract features are unable to make firm predictions about which neurons or regions are performing the computations or how they do it. Our modeling approach not only implicates second-order tactile neurons but differentiates between AMPA-mediated integration (leaning more towards coincidence detection) and NMDA-mediated integration (leaning more towards summation). AMPA-like synapses enabled robust discrimination especially of fine angles within a short time window. Therefore, AMPA inputs may mediate initial rapid computations based on bottom-up input, which could contribute to the fast responses that occur in the context of hand control [15]. NMDA-like synapses refined discrimination and maintained robustness when integrating inputs over longer time windows. Therefore, NMDA inputs may mediate the discrimination of objects based on their macro-geometric features – for example, discriminating between your house and car key when searching in your pocket. Our network models also suggest a tendency for sparseness and the involvement of a small set of key connections between first-order and second-order neurons, supporting previous empirical work [29] and suggesting that imposing a sparseness constraint on the network weights may improve network performance [31]. Previous studies also showed opposing areas of sensitivity in the receptive fields of cortical neurons [32]. Our models predict similar properties for second-order neurons, whereby key connections would be anticorrelated between oppositely-tuned neurons.

Methods

Electrophysiology data. We used microneurography data of spike recordings from first-order tactile neurons, which was previously published [6]. The data consisted of 19 fast-adapting type 1 (FA-1) neurons from 13 human subjects. We utilized 17 of the 19 neurons, omitting one neuron whose receptive field was larger than the inter-stimulus spacing, and one neuron that had a low stimulus/non-stimulus response ratio. The recorded neurons innervated the glabrous skin of the index, long or ring finger. Neurons were stimulated via a rotating drum embossed with dots and edges at different orientations.

First-order tactile neuron models. Model neurons innervated a subset of model mechanoreceptors in a patch of skin modeled as a grid of mechanoreceptors located at 0.15 mm intervals [4] (Figure 1A). Model mechanoreceptor output decreased with the distance from stimulus, following a sigmoidal function:

$$(1) \qquad O_{MR} = \begin{cases} w_{MR} \cdot (1 - 1/(1 + \exp(-(d - 0.05)/0.01)) & \text{d} \leq 0.25 \text{ mm} \\ 0 & \text{d} > 0.25 \text{ mm} \end{cases}$$

Where w_{MR} is the weight of the model mechanoreceptor, and d is the distance of the stimulus from the mechanoreceptor (Figure 1C).

We simulated the model neuron response to moving edge stimuli, at $\Delta t = 1$ ms intervals. Each mechanoreceptor was innervated by its own axon [4] and spikes were initiated at each model mechanoreceptor [23–25,27,33,34]. Spike generation was a function of mechanoreceptor output and the time of the last spike, following a linear relationship between spike rate and mechanoreceptor output (with gain = 1), and saturation at a maximal rate (Figure 1D). The model included spike adaptation, whereby each model neuron axon fired only when input from mechanoreceptor was increasing, and was silent when the input remained the same or decreased (Figure 1E). In addition, spikes from each spiking zone propagated to the other spiking zones, resetting spike initiation and thus resulting in a “winner-take-all” spike rate [23–25]. We used a spike threshold of 0.01 mm stimulus indentation [3]. The model was implemented and simulated in Matlab (Mathworks).

Neuron model optimization. We constrained the models with spike recordings of the response to edges of five different orientations (0, ± 22.5, ± 45˚). The error measure for the goodness of fit was R^2 computed between the recorded and model spike rate curves:

$$(2) \qquad R^2 = \langle (SR_m - SR_o)^2 \rangle / \langle (SR_o - \overline{SR_o})^2 \rangle$$

Where SR_m is the spike rate time-series of the model neuron, and SR_o is the spike rate time-series of the recorded neuron. The error was calculated for each edge orientation and averaged over the orientations to produce a ranking of the model.

We used a genetic algorithm [35–37] to search for the free model parameters, which were the location and the weight of the mechanoreceptors innervated by the model neuron, and the maximal firing rate of the model neuron. The set of possible mechanoreceptor locations was delineated by the area of responsivity of the recorded neuron to a small dot stimulus (Figure 1A, gray). The search limits for the weights were [0,3] times the maximal firing rate of the recorded neuron. The search limits for the maximal firing rate of the model neuron model were [1,1.5] times the maximal firing rate of the recorded neuron. We ran separate optimizations using different number of innervated mechanoreceptors – 5, 10, 20, 30, 40, or 50.

During optimization, a population of 100 models was mutated with a probability of 0.1, and underwent crossover with a probability of 0.1 at each iteration. Models were selected based on how well they fitted the recorded response to the five edges (see above). We implemented the algorithm in Matlab, and optimization runtime of 500 iterations on 4 processors was 1 hour on average.

Model neuron testing. We tested models using the spike recordings in response to edges oriented 30˚. We compared the prediction to null models, in which the mechanoreceptor locations were shuffled across the area of responsivity (see above) and the weights were kept the same. The error measure was R^2, as described above for the fitness.

Nearest-neighbor-distance between model mechanoreceptors. To test whether model mechanoreceptors tended to cluster, we calculated the average nearest-neighbor distance between model mechanoreceptors, as the distance between each mechanoreceptor and the nearest mechanoreceptor, averaged over mechanoreceptors. We compared this value to chance level, calculated using the same measure over sets of mechanoreceptors picked at random within the

receptive field boundary. Randomly-picked sets had the same size as the set of model mechanoreceptors. We similarly compared the nearest-neighbor-distance between mechanoreceptor hotspots (defined as model mechanoreceptors that provided output with a large weight - top 25% of all weights) and chance.

Model network. The simulated tactile network included the first-order neuronal population and second-order tactile neurons (i.e. those neurons in the cuneate or spinal cord). We generated the model first-order neuronal population as variations of the 17 model neurons, by randomizing the mechanoreceptor locations across the area of responsivity while keeping the number and weights of the mechanoreceptors the same. We tiled the model neurons over a 10x10 mm patch of skin, so that they innervated the patch at a uniform density of 140 neurons/cm^2 [2]. This resulted in 292 model neurons innervating mechanoreceptors in the patch. We modeled second-order neuron integration as a weighted sum of PSPs from the first-order population. The connection between first- and second- order neurons exhibit both AMPA and NMDA receptors [38,39]. Therefore, the PSP vector from each first-order neuron was computed by convolving the spike train with PSP waveform, which was the difference of two exponentials:

$$\exp\left(-\frac{t}{\tau_{decay}}\right) - \exp\left(-\frac{t}{\tau_{rise}}\right) \quad (3)$$

Where τ_{rise} = 0.5 ms, and τ_{decay} was either 3 ms as in AMPA receptors [40] or 65 ms as in NMDA receptors [41].

Edge orientation discrimination. The model network faced a task of discriminating between two edges sweeping over the patch of skin, oriented at -θ or θ, where θ = 1, 3, 5, 10, 15 or 20˚. Discrimination was based on the second-order neuron with maximal PSP value over the time series, corresponding to a linear integration with threshold. We trained the model networks using a genetic algorithm to search for the weights between the first-order neurons and second-order neurons [42]. For the genetic algorithm, we used weights limits of [-1,1], a population of 100 models, mutation probability of 0.1, crossover probability of 0.1, and 200 iterations.

We investigated the discrimination accuracy under different levels of additive stimulus noise: 0, 1, 5, or 10%. Noise was added as 0.4 x 0.4 mm patches that varied in amplitude. For example, a noise level of 10% involved addition of noise patches of random amplitudes ranging between -10 and 10% of stimulus amplitude. While the additive noise could reduce stimulus

indentation at some points, we forced the resulting stimulus to be strictly non-negative. We simulated 100 trials for each orientation, where trials differed in the noise added to the stimulus. We picked 50 trials of each orientation at random for training the model networks (100 trials in total), and used the remaining 50 trials of each orientation for testing the model networks. For each task, we generated 20 model networks using different random subsets of training/testing trials. The performance measure was success discrimination rate over trials.

Stimulus presentation time window. We investigated a range of time windows available for the model second-order neurons. In the unlimited window case, edges passed over the skin patch fully from one end to the other. During shorter time windows, the edge passed for a limited time (5, 10, 20, 50, or 100 ms) around the center of the skin patch.

Statistical tests. We determined correlation using Pearson's correlation coefficient. We tested for statistical significance using either paired or two-sample t-test, in Matlab. P-values < 0.05 were deemed significant. When estimating 95% confidence intervals, we used bootstrap estimation of the mean value in Matlab, and corrected for multiple comparisons using Bonferroni method (multiplying the *p* value by the number of comparisons).

Acknowledgements

This work was supported by the Canadian Institutes of Health Research (Foundation Grant to JAP: 353197) and the Government of Ontario (Early Researcher Award to JAP). EH received a postdoctoral fellowship from the Brain and Mind Institute at Western University. JAP received a salary award from the Canada Research Chairs Program.

References

1. Chemnitz A, Dahlin LB, Carlsson IK. Consequences and adaptation in daily life - patients' experiences three decades after a nerve injury sustained in adolescence. BMC Musculoskelet Disord. 2013;14: 252. doi:10.1186/1471-2474-14-252

2. Johansson RS, Flanagan JR. Coding and use of tactile signals from the fingertips in object manipulation tasks. Nat Rev Neurosci. 2009;10: 345–359. doi:10.1038/nrn2621

3. Vallbo AB, Johansson RS. Properties of cutaneous mechanoreceptors in the human hand related to touch sensation. Hum Neurobiol. 1984;3: 3–14.

4. Nolano M, Provitera V, Crisci C, Stancanelli A, Wendelschafer-Crabb G, Kennedy WR, et al. Quantification of myelinated endings and mechanoreceptors in human digital skin. Ann Neurol. 2003;54: 197–205. doi:10.1002/ana.10615

5. Phillips JR, Johansson RS, Johnson KO. Responses of human mechanoreceptive afferents to embossed dot arrays scanned across fingerpad skin. J Neurosci Off J Soc Neurosci. 1992;12: 827–839.

6. Pruszynski JA, Johansson RS. Edge-orientation processing in first-order tactile neurons. Nat Neurosci. 2014;17: 1404–1409. doi:10.1038/nn.3804

7. Suresh AK, Saal HP, Bensmaia SJ. Edge orientation signals in tactile afferents of macaques. J Neurophysiol. 2016;116: 2647–2655. doi:10.1152/jn.00588.2016

8. Jones EG. Cortical and Subcortical Contributions to Activity-Dependent Plasticity in Primate Somatosensory Cortex. Annu Rev Neurosci. 2000;23: 1–37. doi:10.1146/annurev.neuro.23.1.1

9. Gerling GJ, Rivest II, Lesniak DR, Scanlon JR, Wan L. Validating a population model of tactile mechanotransduction of slowly adapting type I afferents at levels of skin mechanics, single-unit response and psychophysics. IEEE Trans Haptics. 2014;7: 216–228. doi:10.1109/TOH.2013.36

10. Sripati AP, Bensmaia SJ, Johnson KO. A continuum mechanical model of mechanoreceptive afferent responses to indented spatial patterns. J Neurophysiol. 2006;95: 3852–3864. doi:10.1152/jn.01240.2005

11. Lesniak DR, Gerling GJ. Predicting SA-I mechanoreceptor spike times with a skin-neuron model. Math Biosci. 2009;220: 15–23. doi:10.1016/j.mbs.2009.03.007

12. Johansson RS, Birznieks I. First spikes in ensembles of human tactile afferents code complex spatial fingertip events. Nat Neurosci. 2004;7: 170–177. doi:10.1038/nn1177

13. Rongala UB, Spanne A, Mazzoni A, Bengtsson F, Oddo CM, Jörntell H. Intracellular Dynamics in Cuneate Nucleus Neurons Support Self-Stabilizing Learning of Generalizable Tactile Representations. Front Cell Neurosci. 2018;12. doi:10.3389/fncel.2018.00210

14. Saal HP, Delhaye BP, Rayhaun BC, Bensmaia SJ. Simulating tactile signals from the whole hand with millisecond precision. Proc Natl Acad Sci. 2017;114: E5693–E5702. doi:10.1073/pnas.1704856114

15. Pruszynski JA, Flanagan JR, Johansson RS. Fast and accurate edge orientation processing during object manipulation. eLife. 2018;7: e31200. doi:10.7554/eLife.31200

16. Zhao CW, Daley MJ, Pruszynski JA. Neural network models of the tactile system develop first-order units with spatially complex receptive fields. PLOS ONE. 2018;13: e0199196. doi:10.1371/journal.pone.0199196

17. Donoho DL. Compressed sensing. IEEE Trans Inf Theory. 2006;52: 1289–1306. doi:10.1109/TIT.2006.871582

18. Carlson NL, Ming VL, DeWeese MR. Sparse Codes for Speech Predict Spectrotemporal Receptive Fields in the Inferior Colliculus. PLOS Comput Biol. 2012;8: e1002594. doi:10.1371/journal.pcbi.1002594

19. Barranca VJ, Kovačič G, Zhou D, Cai D. Sparsity and Compressed Coding in Sensory Systems. PLOS Comput Biol. 2014;10: e1003793. doi:10.1371/journal.pcbi.1003793

20. Ganguli S, Sompolinsky H. Compressed Sensing, Sparsity, and Dimensionality in Neuronal Information Processing and Data Analysis. Annu Rev Neurosci. 2012;35: 485–508. doi:10.1146/annurev-neuro-062111-150410

21. Caron SJC, Ruta V, Abbott LF, Axel R. Random convergence of olfactory inputs in the Drosophila mushroom body. Nature. 2013;497: 113–117. doi:10.1038/nature12063

22. Zhang Y, Sharpee TO. A Robust Feedforward Model of the Olfactory System. PLOS Comput Biol. 2016;12: e1004850. doi:10.1371/journal.pcbi.1004850

23. Horch KW, Whitehorn D, Burgess PR. Impulse generation in type I cutaneous mechanoreceptors. J Neurophysiol. 1974;37: 267–281. doi:10.1152/jn.1974.37.2.267

24. Fukami Y. Interaction of impulse activities originating from individual Golgi tendon organs innervated by branches of a single axon. J Physiol. 1980;298: 483–499.

25. Lesniak DR, Marshall KL, Wellnitz SA, Jenkins BA, Baba Y, Rasband MN, et al. Computation identifies structural features that govern neuronal firing properties in slowly adapting touch receptors. eLife. 2014;3: e01488. doi:10.7554/eLife.01488

26. Maass W. To Spike or Not to Spike: That Is the Question. Proc IEEE. 2015;103: 2219–2224. doi:10.1109/JPROC.2015.2496679

27. Goldfinger MD, Fukami Y. Interaction of activity in frog skin touch afferent units. J Neurophysiol. 1981;45: 1096–1108. doi:10.1152/jn.1981.45.6.1096

28. Jörntell H, Bengtsson F, Geborek P, Spanne A, Terekhov AV, Hayward V. Segregation of Tactile Input Features in Neurons of the Cuneate Nucleus. Neuron. 2014;83: 1444–1452. doi:10.1016/j.neuron.2014.07.038

29. Bengtsson F, Brasselet R, Johansson RS, Arleo A, Jörntell H. Integration of Sensory Quanta in Cuneate Nucleus Neurons In Vivo. PLOS ONE. 2013;8: e56630. doi:10.1371/journal.pone.0056630

30. Hayward V, Terekhov AV, Wong S-C, Geborek P, Bengtsson F, Jörntell H. Spatio-temporal skin strain distributions evoke low variability spike responses in cuneate neurons. J R Soc Interface. 2014;11: 20131015. doi:10.1098/rsif.2013.1015

31. Hay E, Ritter P, Lobaugh NJ, McIntosh AR. Multiregional integration in the brain during resting-state fMRI activity. PLoS Comput Biol. 2017;13: e1005410. doi:10.1371/journal.pcbi.1005410

32. DiCarlo JJ, Johnson KO, Hsiao SS. Structure of Receptive Fields in Area 3b of Primary Somatosensory Cortex in the Alert Monkey. J Neurosci. 1998;18: 2626–2645. doi:10.1523/JNEUROSCI.18-07-02626.1998

33. Eagles JP, Purple RL. Afferent fibers with multiple encoding sites. Brain Res. 1974;77: 187–193.

34. Lindblom Y, Tapper DN. Integration of impulse activity in a peripheral sensory unit. Exp Neurol. 1966;15: 63–69.

35. Hay E, Hill S, Schürmann F, Markram H, Segev I. Models of neocortical layer 5b pyramidal cells capturing a wide range of dendritic and perisomatic active properties. PLoS Comput Biol. 2011;7: e1002107. doi:10.1371/journal.pcbi.1002107

36. Hay E, Schürmann F, Markram H, Segev I. Preserving axosomatic spiking features despite diverse dendritic morphology. J Neurophysiol. 2013;109: 2972–2981. doi:10.1152/jn.00048.2013

37. Druckmann S, Banitt Y, Gidon AA, Schürmann F, Markram H, Segev I. A novel multiple objective optimization framework for constraining conductance-based neuron models by experimental data. Front Neurosci. 2007;1. doi:10.3389/neuro.01.1.1.001.2007

38. Soto C, Aguilar J, Martín-Cora F, Rivadulla C, Canedo A. Intracuneate mechanisms underlying primary afferent cutaneous processing in anaesthetized cats. Eur J Neurosci. 2004;19: 3006–3016. doi:10.1111/j.0953-816X.2004.03432.x

39. Kus L, Saxon D, Beitz AJ. NMDA R1 mRNA distribution in motor and thalamic-projecting sensory neurons in the rat spinal cord and brain stem. Neurosci Lett. 1995;196: 201–204.

40. Hestrin S. Activation and desensitization of glutamate-activated channels mediating fast excitatory synaptic currents in the visual cortex. Neuron. 1992;9: 991–999.

41. Rhodes P. The properties and implications of NMDA spikes in neocortical pyramidal cells. J Neurosci Off J Soc Neurosci. 2006;26: 6704–6715. doi:10.1523/JNEUROSCI.3791-05.2006

42. Such FP, Madhavan V, Conti E, Lehman J, Stanley KO, Clune J. Deep Neuroevolution: Genetic Algorithms Are a Competitive Alternative for Training Deep Neural Networks for Reinforcement Learning. ArXiv171206567 Cs. 2017; Available: http://arxiv.org/abs/1712.06567